Generation of high-power terahertz pulses by tilted-pulse-front excitation and their application possibilities

János Hebling,[1,2,]* Ka-Lo Yeh,[1] Matthias C. Hoffmann,[1] Balázs Bartal,[2] and Keith A. Nelson[1]

[1]*Department of Chemistry, Massachusetts Institute of Technology, Cambridge, Massachusetts 02139, USA*
[2]*Department of Experimental Physics, University of Pécs, 7624 Hungary*
*Corresponding author: hebling@mit.edu

The principles and most-recent results of high-power THz generation through optical rectification using a tilted optical pulse front are described. Single-cycle THz pulses of multimicrojoule energies are generated at kHz repetition rates, and average THz power levels exceeding 1 mW can be generated at kHz–MHz repetition rates. Applications in nonlinear THz spectroscopy and THz coherent control are discussed. © 2008 Optical Society of America

OCIS codes: 190.7110, 190.2620, 260.3090.

1. INTRODUCTION

The rapidly developing field of THz science [1,2] includes advances in various mechanisms for generation of electromagnetic radiation in the 0.1–10 THz range and in the characterization of responses of physical, chemical, and biological materials to such radiation. Nowadays the overwhelming majority of THz research and applications involve THz sources having rather low energy. Although these sources enable applications including imaging and spectral identification of materials, important applications such as single-shot imaging, THz radar, THz–THz pump–probe measurement of dynamics, and THz electron spin resonance generally need more energetic pulses. Free-electron lasers can produce THz pulses with up to 100 μJ of energy [3]. However, access to these large-scale facilities is limited, and shaping of the THz waveform is not generally possible. Until recently, large-aperture photoconductive switches [4] illuminated by ultrashort laser pulses were the only tabletop sources of single-cycle THz pulses with high energy, with values up to 0.8 μJ reported. However, the spectral peak of the pulses generated by this device was below 0.5 THz, and the high-voltage switching involved poses practical challenges and signal/noise limitations. Recently, photoconductive metal–semiconductor–metal (MSM) structures were developed in order to achieve a high accelerating field with only 50 V bias [5]. The peak of the generated THz field was 85 V/cm.

From the point of view of efficiency, simplicity, and diversity of possible applications, optical rectification of ultrashort laser pulses is currently the most promising method [6–9] for generation of high-energy THz pulses. Efficient optical rectification requires the group velocity of the ultrashort laser pulse to be equal to the phase velocity

of the generated THz radiation [10]. To fulfill this requirement, ZnTe is commonly used as nonlinear optical material for optical rectification. But the nonlinear coefficient of this material is much lower than that of $LiNbO_3$. That the THz phase velocity is more than two times smaller than the visible group velocity has hindered THz applications of this material in the past. However, the use of spatially and temporally shifted sequences of optical pulses to form discrete tilted intensity fronts whose effective velocity matched the phase velocity of THz phonon–polaritons in $LiNbO_3$ [11–13] resulted in substantially improved phonon–polariton amplitudes. We proposed [14] a easy method for continuous tilting of the intensity front of the ultrashort excitation pulse to match the THz velocity. Using this velocity matching method we were able to produce THz pulses having 1000 times larger energy [15] than that of THz pulses generated in ZnTe [8] by using the same pump pulse energy.

This paper—after reviewing the properties of the most commonly used electro-optic materials—describes the principle and technique of THz pulse generation by tilted-pulse-front excitation, using the results of calculations based on two models to predict the dependence of the THz pulse energy and the electric field strength on the crystal length and temperature. It also presents the most-recent experimental results of high-energy and high-average-power single-cycle THz pulse generation. Furthermore, it considers the combination of tilted-pulse-front excitation with femtosecond pulse shaping in order to effectively produce high-power arbitrarily shaped THz waveforms for quantum control experiments and THz signal processing. Finally, it gives a short summary of the emerging application possibilities of these shaped high-energy THz pulses.

2. COMPARISON OF ELECTRO-OPTIC MATERIALS

Optical rectification of ultrashort laser pulses can be considered a result of difference-frequency mixing among the spectral components contained within the ultrashort-pulse bandwidth. To compare the suitability of different nonlinear optical crystals for optical rectification, let us start from the formula given in [16]. This formula describes the efficiency of difference-frequency generation by long plane wave pulses in the absence of pump absorption or depletion, taking into account the effect of THz absorption. For phase-matched conditions the formula reads as

$$\eta_{THz} = \frac{2\omega^2 d_{eff}^2 L^2 I}{\varepsilon_0 n_{NIR}^2 n_{THz} c^3} \exp[-\alpha_{THz}L/2] \cdot \frac{\sinh^2[\alpha_{THz}(L/4)]}{[\alpha_{THz}L/4]^2}. \tag{1}$$

Here ω is the angular difference (THz) frequency, d_{eff} the effective nonlinear coefficient, I the intensity of the near-infrared (NIR) light, ε_o the vacuum permittivity, c the velocity of light in vacuum, L the length of the nonlinear crystal, α_{THz} the intensity absorption coefficient for the THz radiation, and n_{NIR} and n_{THz} the refraction indices in the NIR and THz range, respectively. For negligible absorption ($\alpha_{THz}L \ll 1$) Eq. (1) is reduced to

$$\eta_{THz} = \frac{2\omega^2 d_{eff}^2 L^2 I}{\varepsilon_0 n_{NIR}^2 n_{THz} c^3}. \tag{2}$$

In contrast, for large absorption ($\alpha_{THz}L \gg 1$), Eq. (1) simplifies to

$$\eta_{THz} = \frac{8\omega^2 d_{eff}^2 I}{\varepsilon_0 n_{NIR}^2 n_{THz} c^3 \alpha_{THz}^2}. \tag{3}$$

The consequence is obvious: it is useless to choose a crystal length greater than the penetration depth of the THz radiation α_{THz}^{-1}. Only those THz photons that are produced within a region $L_{eff} = \alpha_{THz}^{-1}$ of the exit surface of the crystal can significantly contribute to the THz emission.

According to Eqs. (2) and (3) it is possible to introduce two figures of merit (FOMs) of the nonlinear crystal used for optical rectification [17,18] defined by

$$FOM_{NA} \equiv \frac{d_{eff}^2 L^2}{n_{NIR}^2 n_{THz}}, \tag{4}$$

$$FOM_A \equiv \frac{4 d_{eff}^2}{n_{NIR}^2 n_{THz} \alpha_{THz}^2}. \tag{5}$$

The FOM_{NA} and FOM_A values are measures of the energy conversion efficiencies for optical rectification in weakly and strongly absorbing crystals, respectively. It should be noticed, however, that for approximately 100 fs long pump pulses the crystal length has to be limited to $1-2$ mm because of dispersion in the NIR and, even more important, in the THz range. Because of this, and in order to get a unique parameter, it is useful to define a FOM equal to FOM_A if α_{THz} is larger than 5 cm^{-1}, and equal to FOM_{NA} with $L=2$ mm in Eq. (4) for smaller α_{THz} values.

We have collected the most relevant parameters of nonlinear optical materials frequently used for optical rectification in Table 1. The clamped electro-optic coefficients r (not shown) and the NIR refractive index values n_{NIR} are used to calculate the nonlinear optical coefficient for optical rectification d_{eff} (second column) according to [36]

$$d_{eff} = -n_{NIR}^4 r/4, \tag{6}$$

since directly measured d_{eff} values are available only for very few materials. For such materials (e.g., GaAs) the measured and calculated d_{eff} values agree very well.

According to Table 1, at room temperature DAST has the highest FOM value. This material has been used recently to generate THz pulses with 50 kV/cm focused field strength [37]. This result actually was achieved by using 25 μJ excitation pulses at 1.55 μm, which suggests that the FOM value under the reported conditions was only 6.6 pm^2 cm^2/V^2 [33]. CdSe has the third highest FOM value; however, we are not aware of any reported use of this material for optical rectification. The reason is that CdSe is strongly absorbing at the 800 nm output of the Ti:sapphire laser, the most commonly used ultrashort pulse source. ZnTe, which is the most commonly used electro-optic crystal for optical rectification and electro-optic sampling, has only the fourth highest FOM value. The reason for the widespread application of this material is that for Ti:sapphire pumping, collinear velocity match-

Table 1. Properties of a Few Materials Suitable for Optical Rectification[a]

Material	d_{eff} (pm/V)	n_{800nm}^{gr}	n_{THz}	$n_{1.55\mu m}^{gr}$	α_{THz} (cm^{-1})	FOM (pm^{2}cm^2/V^2)
CdTe	81.8 [19]		3.24 [20]	2.81 [21]	4.8 [20]	11.0
GaAs	65.6 [19]	4.18 [22]	3.59 [23]	3.56 [22]	0.5 [22]	4.21
GaP	24.8 [24]	3.67 [25]	3.34 [25]	3.16 [25]	0.2 [25]	0.72
ZnTe	68.5 [19]	3.13 [26]	3.17 [20]	2.81 [21]	1.3 [20]	7.27
GaSe	28.0 [27]	3.13 [28]	3.27 [29]	2.82 [28]	0.5 [29]	1.18
sLiNbO$_3$	168 [19]	2.25 [30]	4.96 [31]	2.18 [30]	17 [32]	18.2
sLN 100 K					4.8 [31]	48.6
DAST	615 [33]	3.39 [34]	2.58 [35]	2.25 [34]	50 [35]	41.5

[a]Except for DAST (4-*N*,*N*-dimethylamino-4′-*N*′-methyl stilbazolium tosylate), the THz index n_{THz} and absorption coefficient α_{THz} are given for 1 THz. For DAST these values are given for 0.8 THz, since this material has an absorption peak at 1 THz. For this material the value of d strongly depends on the excitation wavelength. The indicated d and FOM values are given for 800 nm. For 1.55 μm in DAST these values are 2.5 and 6.3 times smaller, respectively. All values are for room temperature except those for stochiometric LiNbO$_3$ (sLN) at 100 K. GaP, gallium phosphide.

ing between the pump pulse and the THz radiation is approximately fulfilled. Stochiometric LiNbO$_3$ (sLN) has the second highest FOM, its value more than two times larger than that of ZnTe. As mentioned above, however, the energy of THz pulses (even at room temperature) generated using this material was orders of magnitude higher [15] than that for ZnTe for the same pump energy. The reason for this is that the relatively small bandgap of the semiconductors makes possible two-photon absorption of the pump pulses at 800 nm [8,9,38]. The key point here is not the loss of pump intensity but rather the strong THz absorption due to carriers created by the two-photon absorption. The bandgap of sLN is significantly higher [39], excluding two-photon absorption at 800 nm. Because of this, much higher pump intensity can be used for sLN than for semiconductors, resulting in much higher THz pulse energy and higher conversion efficiency.

Concerning sLN, it is important to notice that LiNbO$_3$ has strong photorefraction. However, this effect can be suppressed by doping, for example with Mg. According to Z-scan measurements, the necessary doping level depends on the composition. For the more common congruent LN (cLN), it is above 5%, while for sLN it is less than 0.7% [40]. The THz absorption coefficient α_{THz} depends on the stoichiometry and the Mg doping level [31]. Fortunately (but not accidentally), for both cLN and sLN α_{THz} is smallest for Mg doping levels just above the threshold for suppression of photorefraction. sLN has lower THz absorption than cLN. The difference is most significant at low temperature [31]. As indicated in Table 1, at 100 K α_{THz} becomes so small for sLN that its FOM becomes about five times larger than that of the best semiconductor and also becomes larger than that of DAST.

As for any nonlinear optical frequency conversion process involving a long interaction length, for optical rectification a phase-matching condition between the frequency components involved has to be fulfilled in order to obtain the largest conversion efficiency. Specifically, the phase-matching condition requires the group velocity of the pump pulse to be equal to the phase velocity of the generated THz radiation [10]:

$$v_{NIR}^{gr} = v_{THz}. \tag{7}$$

This should further require the equality of the corresponding indices:

$$n_{NIR}^{gr} = n_{THz}. \tag{8}$$

According to Table 1, however, $n_{THz} > n_{NIR}^{gr}$ for 800 nm NIR pump pulses in the cases of GaSe and LiNbO$_3$. Furthermore, for 1.55 μm pump pulses (i.e., Er^{3+} fiber laser output) $n_{THz} > n_{NIR}^{gr}$ in the case of all the considered materials. Consequently it is important to develop a velocity matching technique that is applicable in the very frequent case of a THz index larger than the NIR group index. It is obvious that velocity matching cannot be achieved based on birefringence in the isotropic semiconductors (all those in Table 1 except GaSe) or in LN for which the birefringence is much less than the difference between the NIR and THz (far-IR) indices. It is also important to notice that although in periodically poled material (e.g., periodically poled LN) quasi-phase matching

can be realized and relatively high conversion efficiency (10^{-5}) can be reached at low (18 K) temperature [41], velocity matching is not fulfilled in this case. Consequently, the periodically poled crystals create a multiple-cycle THz pulse instead of a single cycle, and the efficiency cannot be as high as in the case of velocity matching since the THz components generated in the different domain pairs exit the crystal temporally separated, with no constructive interference.

3. PRINCIPLE AND REALIZATION OF TILTED-PULSE-FRONT EXCITATION

In 2002 we suggested tilting of the intensity front of the pump pulse to reach velocity matching [14]. The operation of this method is illustrated in Fig. 1(a). According to Huygens' principle [42], the THz radiation (in phonon–polariton form inside the crystal) that is excited by the tilted pulse front of the NIR pump propagates perpendicularly to this front with a velocity v_{THz}. Consequently the angle between the propagation direction of the THz radiation and the propagation direction of the pump pulse will be the same as the tilt angle γ of the pulse front relative to the phase front of the pump (which is perpendicular to its propagation direction). Because of this, the magnitudes of the velocities have to satisfy Eq. (9) instead of Eq. (7):

$$v_{NIR}^{gr} \cos \gamma = v_{THz}. \tag{9}$$

If $v_{NIR}^{gr} \geq v_{THz} (n_{NIR}^{gr} \leq n_{THz})$ then this modified velocity matching condition can be easily fulfilled by an appropriate choice of the angle γ. It is also possible to derive
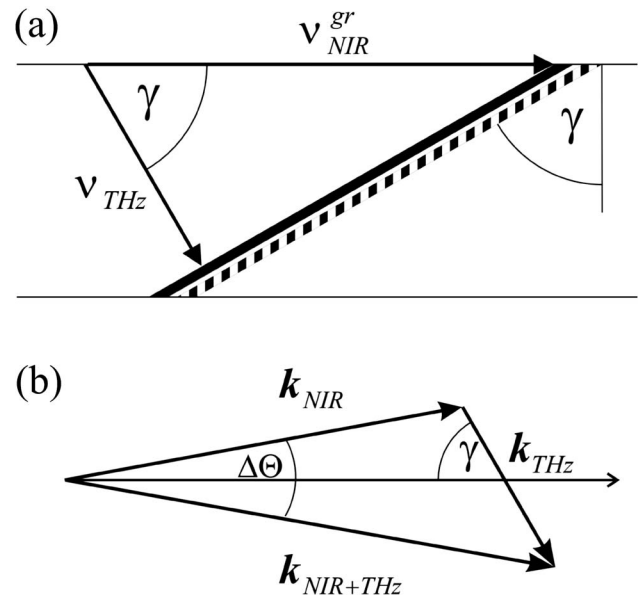

Fig. 1.   Illustration of velocity matching using tilted-pulse-front excitation. (a) THz phonon–polariton wave (bold line) generated in the LN crystal by the tilted intensity front of the pump pulse (dashed bold line) propagates perpendicular to the THz phase front. In order for the two fronts to remain in phase during propagation, the projection of the pump pulse velocity vector v_{NIR}^{gr} along the direction of the polariton (THz radiation) propagation vector should be equal to the magnitude of THz phase velocity v_{THz}.   (b) Wave-vector diagram for difference-frequency generation.

Eq. (9) by considering the optical rectification as a difference-frequency generation process. The ultrashort pump pulse contains components covering a wide frequency range. Pulse front tilting of a light beam necessarily leads to angular dispersion [43]: components with different frequencies propagate in slightly different directions. Considering two frequency components $\omega_{NIR+THz}$ and ω_{NIR}, efficient generation of radiation with frequency ω_{THz} by difference frequency mixing requires fulfillment of the well-known phase-matching condition [see the wave vector diagram depicted in Fig. 1(b)]:

$$\Delta\mathbf{k} = \mathbf{k}_{NIR+THz} - \mathbf{k}_{NIR} - \mathbf{k}_{THz} = 0, \tag{10}$$

where the $\mathbf{k}$'s are the wave vectors of the corresponding frequency components. The connection between the pulse front tilt γ and the angular dispersion $d\Theta/d\omega$ for a material with refraction index n_{NIR} is given by [43]:

$$\tan\gamma = -\frac{n_{NIR}}{n_{NIR}^{gr}}\omega\frac{d\Theta}{d\omega}, \tag{11}$$

where $n_{NIR}^{gr} = n_{NIR} + \omega(dn_{NIR}/d\omega) = c/v_{NIR}^{gr}$.

Using Eq. (11), it is easy to show that for small values of $\Delta\Theta$, the inclination angle of $\mathbf{k}_{THz}$ from the average direction of $\mathbf{k}_{NIR}$ and $\mathbf{k}_{NIR+THz}$ is the same as the pulse front tilt angle γ. Therefore the two pictures used to describe THz pulse excitation by ultrashort pulses with a tilted pulse front, based on Huygens' principle or wave-vector conservation, predict the same propagation direction for the created THz beam. In our experiments, described later, the full angular spread of the light beam $\Delta\Theta$ was about $2°-5°$, while γ was $63°-65°$.

It is also interesting to compare the tilted-pulse-front excitation setup to the electro-optic Cherenkov generation geometry [44–46], which was used first for THz generation by optical rectification of ultrashort light pulses. Comparing Figs. 2(a) and 2(b), it is obvious that the Cherenkov cone with the indicated angle Θ_C,

$$\Theta_C = \cos^{-1}(v_{THz}^{ph}/v_{NIR}^{gr}), \tag{12}$$

satisfies Eq. (9) with $\Theta_C = \gamma$. In this respect electro-optic Cherenkov generation is similar to the tilted-pulse-front excitation, but with several disadvantages. One is that the generated THz radiation propagates along a cone [see
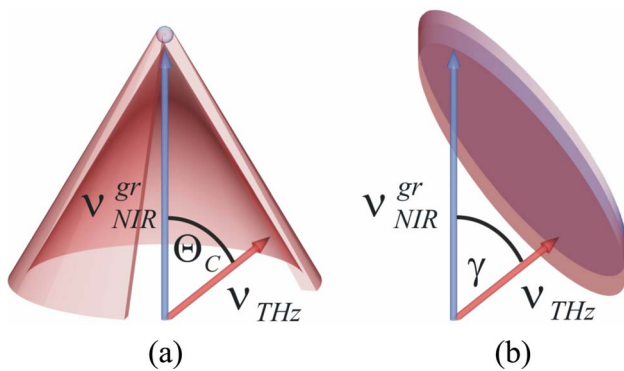

Fig. 2. (Color online) (a) For the Cherenkov geometry, the THz radiation is emitted as a cone. Velocity matching [Eq. (9)] is satisfied, but the pump spot size has to be small. (b) Tilted-pulse-front excitation creates a plane THz wave, and the spot size and THz energy can be scaled up.

Fig. 2(a)] with the angle Θ_C. Such a propagation characteristic makes it very difficult to collect the THz radiation for applications. The situation can be improved through the use of an optical beam that is cylindrically focused to form a line rather than point source, in which case THz plane waves are generated [11–13,47]. However, even in this case the THz radiation generated at a given time during the traversal of the line source through the crystal cannot interact with the radiation generated later, while for an extended beam with a tilted pulse front, a plane wave is generated in which the THz amplitude components created at different times and lateral positions superpose on each other in the nonlinear medium, resulting in enhanced conversion efficiency. The second disadvantage of the electro-optic Cherenkov geometry is that it can produce THz radiation at a specified wavelength λ_{THz} only if the lateral extension (beam waist) w of the pump light pulse is considerably smaller than the wavelength [46]:

$$w \ll \lambda_{THz}. \tag{13}$$

Because of this the energy of the THz emission cannot be increased by simultaneously increasing the pump spot size and energy, contrary to the case of the tilted-pulse-front excitation setup. Essentially, the tilted pulse front geometry allows the pump light to be spread out spatially while the THz responses to the disparate optical field components superpose constructively and remain sharply peaked, typically in a near-single-cycle pulse. The tilted pulse front therefore enables the use of high optical pulse energy while averting unwanted nonlinear optical effects and building up a large THz field amplitude and THz pulse energy.

The spreading of the optical pump light also motivated the use of discrete, spatially and temporally shifted pump pulses [11–13], but since THz damping occurs between as well as within the irradiated regions, this approach yields considerably lower overall THz conversion efficiency.

In the case of sLN, to achieve velocity matching by tilted-pulse-front excitation a tilt angle as large as 63° is necessary inside the crystal because n_{THz} is much higher than the NIR group index (see Table 1). Since the tilt angle of the intensity front of the pump pulse decreases on entry into the crystal, according to Eq. (14),

$$\tan\gamma = (1/n_{NIR}^{gr})\tan\gamma^*, \tag{14}$$

the tilt angle outside of the crystal, γ^*, has to be 78°. The simplest method to create such high tilt angle is diffraction of the pump beam off a grating.

In our recent THz generation experiments [14,15,18,38,48–51] we used the experimental setup shown schematically in Fig. 3. (In [46] a two-lens telescope with a focal length ratio of 2:1 was used, instead of a single lens, to relay imaging the pump spot on the grating into the sLN crystal.) As a source of ultrashort pump pulses, first a 200 kHz repetition-rate Ti:sapphire oscillator–amplifier laser system supplying 170 fs pump pulses with up to 3 μJ energy was used [14,18,48]. Later a 1 kHz laser system with 220 fs duration and 0.5 mJ energy pulses was used [15]. Very recently a 1 kHz system delivering sub-100-fs pulses with 6 mJ [50] and a 10 Hz
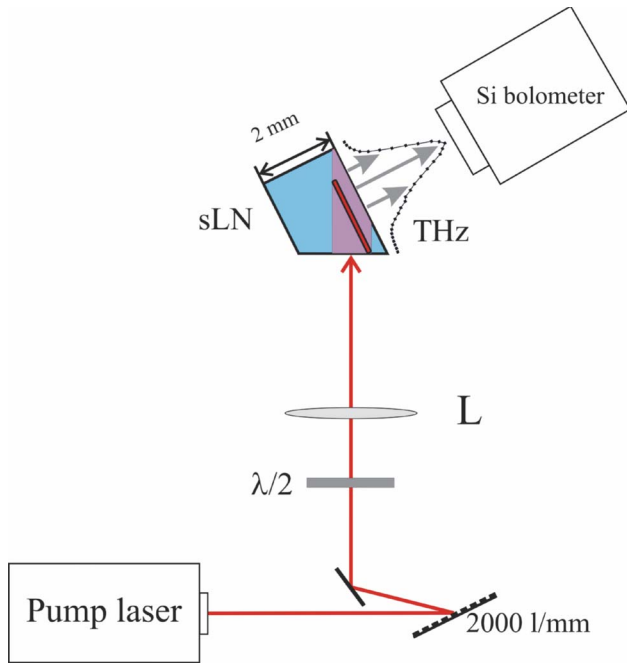
Fig. 3.   (Color online) Experimental setup for THz generation by tilted-pulse-front excitation. L, lens; l/mm, lines/mm.

system delivering 130 fs pulses with 20 mJ [51] were employed as pump sources. A 2000 line/mm grating was applied to tilt the intensity front of the pump pulses. A $\lambda/2$ plate turned the horizontal polarization (for which the efficiency of the grating is high) of the pump beam to vertical, aligned with the optic axis of the $LiNbO_3$ crystal. This is necessary for efficient THz generation, since in $LiNbO_3$ the d_{33} electro-optic tensor component has the highest value. An $f=60$ mm lens was used to image the pump spot at the grating into the $LiNbO_3$ crystal. Typically a demagnification of 2 was used, creating a two-times-smaller spot in the crystal than at the grating and a two times increase of the tangent of the tilt angle. In the case of 1.035 μm (Yb laser) pumping, the demagnification was close to 1 [38].

Since pulse front tilting of a light beam necessarily leads to angular dispersion [43], after diffraction off the grating the different pump frequency components propagate in different directions. Because of this, the pulse front tilt decreases and the pulse duration lengthens during propagation [52]. In the image plane, however, the original pulse duration is reconstructed. The transverse size of the beam is decreased by the demagnification, but the delay between the two sides of the beam remains that created by the grating. Because of this the tangent of the tilt angle is increased by the demagnification. Because of imaging errors, the reconstruction is not perfect, but according to ray-tracing calculations [53], for a spot size smaller than 1 mm on the $LiNbO_3$ crystal the remaining distortion of the pump pulse is negligible. In some of our very recent experiments the spot size is larger than 5 mm. In these cases the temporal distortions can be comparable with the period of the generated THz pulse, resulting in degradation of the THz generation efficiency. Such degradation can be reduced in the future through optimized imaging setups.

At first we employed stoichiometric $LiNbO_3$ (sLN) crystal with a 2 mol.% doping level [48], but in later experiments we used sLN with only 0.6 mol.% Mg doping, since we found [40] that the reduced doping level is still sufficient to prevent photorefractive damage, while its THz absorption is reduced [31]. Most of the experiments were done at room temperature, but measurements at lower temperature were also performed. In the first experiments a calibrated liquid-He-cooled Si bolometer was used to measure the average power of the THz pulses. Later a less sensitive Microtech Instruments pyroelectric powermeter was used to measure the higher average power of the THz pulses. Very recently a Scientech Vector HR P09 pyroelectric laser energymeter was used to measure the energy of the strongest THz pulses.

4. MODEL CALCULATION

Two different models were used to predict the mean behavior of the tilted-pulse-front generation method and the generated THz pulses. One is a position-dependent (two-dimensional) model. This can be used to predict the spatial dependence and spatial distribution of the THz pulses. However, since this model does not include the dispersion of the THz radiation, it does not predict well the temporal shape of the THz pulses. For this purpose a one-dimensional numerical method was used, which takes into account the dispersion and absorption of the generated THz pulses during propagation inside the nonlinear crystal. Finite-difference time-domain numerical simulations of polariton generation and propagation [54] are probably best suited for an accurate description of the process, and these are being attempted in ongoing work.

A. Model for Spatial Dependence

A simple and expedient position-dependent model can be obtained [15] starting from the analytical solution of THz pulse generation by a line source [46]. According to Eq. (19) of [46], the THz electric field strength generated by an ultrashort light pulse propagating into the +z direction and focused to a line with a beam waist w in the y direction and infinite in the x direction can be described as

$$E(y,z,t) \propto \frac{\cot \theta_C}{\tau^2(1+q^2)} \xi e^{-\xi^2}, \qquad (15)$$

with

$$\xi = \frac{|y|\tan \theta_C + z - v_{NIR}^{gr}t}{v_{NIR}^{gr}\tau\sqrt{1+q^2}}, \quad \text{and} \quad q = \frac{w \tan \theta_C}{v \tau},$$

where the FWHM pulse duration is 1.665τ. For a spatially extended source, as in tilted-pulse-front excitation, the generated THz field can be obtained by convoluting the intensity distribution in the $y-z$ plane with the electric field distribution given by Eq. (15). Figure 4 displays results obtained assuming sLN as the nonlinear crystal and a 250 fs duration pump pulse. According to Fig. 4(a), a line source generates two plane waves that propagate in directions determined by the Cherenkov angle Θ_C satisfying Eq. (12). For tilted-pulse-front excitation only one plane wave superposes constructively, while the other, for
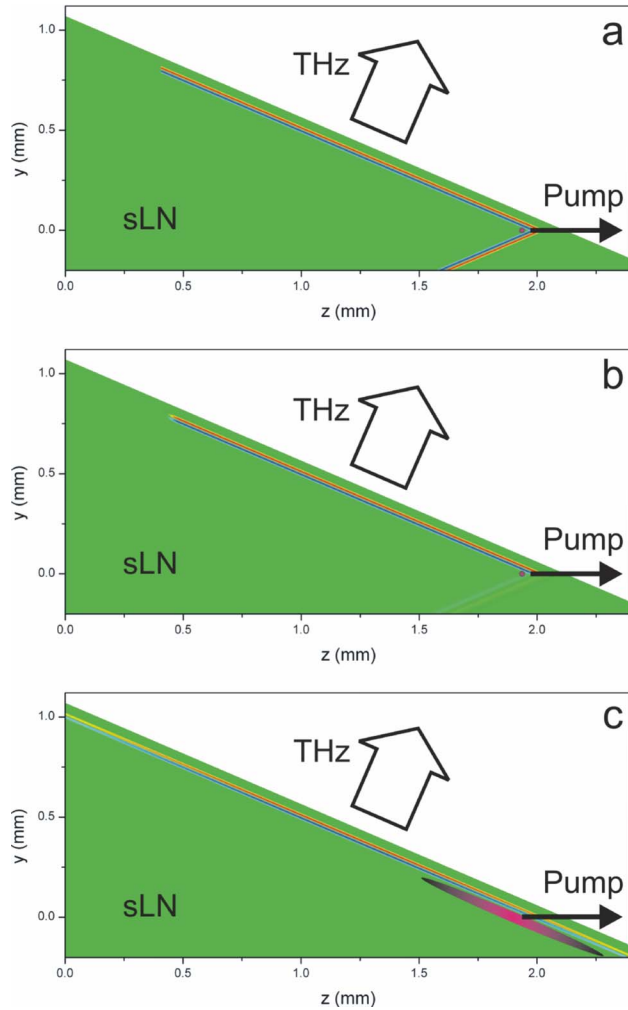
Fig. 4. (Color online) Simulated electric field distribution of THz pulses (just before leaving the crystal) generated in a 2 mm long sLN crystal by a 250 fs pump pulse (a) focused to a 5 μm wide line perpendicular to the figure, (b) with tilted-pulse-front and a spot sizes (measured parallel to the y axis) of 20 μm and (c) of 1 mm. For the sake of visibility the pump pulse is indicated 0.06 mm back from its real position.

which the phase front should not be parallel to the pump pulse front, is suppressed. This suppression is so effective that even for an only 20 μm wide pump spot, i.e., for hardly any pulse front tilt [see Fig. 4(b)], the intensity of that wave is less than 20% of the favored wave. For a 1 mm pump spot size (see Fig. 4(c)) the suppressed wave cannot be observed.

The development of the THz radiation during the propagation of the pump pulse through the crystal is different for the line focusing and the tilted-pulse-front geometry. In the case of line focusing the THz field strength and the intensity are constant, and only the area of the THz wave, and consequently its integrated energy, increases (linearly) as time elapses and the pump pulse traverses the crystal (see triangles in Fig. 5). In contrast, for tilted-pulse-front excitation the electric field strength increases. Since the intensity is proportional to the square of the field strength, the intensity and the THz pulse energy show a superlinear dependence (see squares in Fig. 5). For a given pump energy, the values of the THz
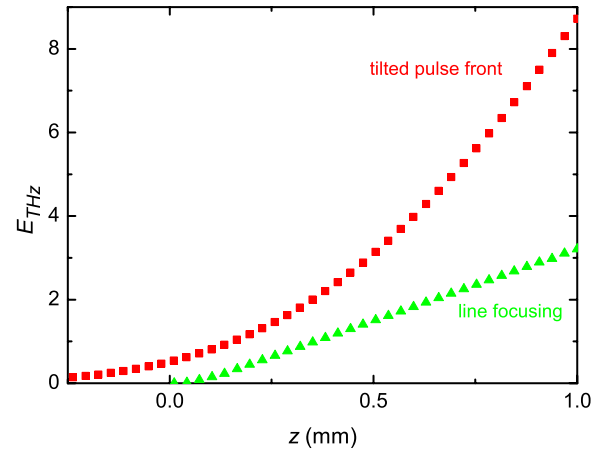

Fig. 5. (Color online) Energy of THz pulses (in arbitrary units) generated in a 1 mm long crystal versus position of the pump pulse inside the crystal for line focusing (triangles) and tilted-pulse-front (squares) excitation assuming 5 μm and 1 mm pump widths, respectively. The energy values were obtained by calculating the square of the field distribution and integrating on the y−z plane. For negative z values the maximum of the tilted pulse front is outside of the crystal.

energies generated for a given position in Fig. 5 by the two excitation setups depend on the pump spot sizes. For line focusing, the THz pulse energy (as well as bandwidth) drops rapidly with increasing line width w even for constant pump intensity (increasing pump energy), since the higher-frequency THz field components generated at the different points (y direction in Fig. 4) cancel each other. Assuming a 20 μm beam width instead of 5 μm, for example, results in a nearly ten times drop in the THz energy according to the calculations.

In contrast, tilted-pulse-front excitation benefits from a larger excitation spot size over which THz field superposition occurs. This is illustrated in Fig. 6. The solid curve is the result of a calculation assuming a 2 mm long crystal (in the z direction). Since in the calculation the pump intensity was kept constant, a larger pump width means a larger pump energy. Because of this, a constant efficiency would correspond to a line starting from the origin. This is illustrated by the dashed line. To make clearer the
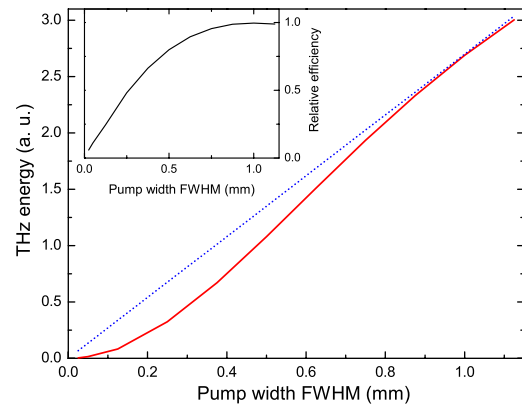

Fig. 6. (Color online) Calculated THz energy versus pump width for constant intensity (solid curve). The dashed line corresponds to a constant efficiency. The inset is the ratio of the two curves, indicating the change of the normalized efficiency with the pump width.

change of the normalized efficiency with the beam width, the inset shows the ratio of the values from the solid and dashed curves. According to this the efficiency increases strongly up to about 0.5 mm pump width. So the tilted-pulse-front excitation is effective for large pump pulse energy, when a large spot size has to be used in order to avoid damage to the nonlinear crystal. The reason for the strong drop in efficiency at smaller than 0.5 mm pump width (using a 2 mm long crystal) is that, similarly to the case of line focusing and as a result of the lateral propagation of the THz radiation, the field created at the first part of the crystal will not meet the field created at the last part of the crystal. So the energy of the THz radiation is summed up, but not the field. When the field can be summed up (for large beam sizes) by constructive interference, the THz energy increases approximately with the square of the propagation length, (see squares in Fig. 5) but it increases only linearly (see triangles in Fig. 5) if it is the energy that is summed up.

B. Model Including Absorption and Dispersion

Since the nonlinear crystals have significant dispersion and absorption in the THz range, there is a need for calculations using more realistic models that take these effects into account. Such a model, which is also calculation-time effective, was described recently [18,49]. A summary of this model is the following. Assuming a transform-limited pump pulse with duration τ_p propagating in the z direction with velocity v_{gr} (note that since this model is not two dimensional in space, the projection of v_{NIR}^{gr} in the direction of the THz pulse propagation in Fig. 1 is considered, its direction is chosen to be the z axis, and its amplitude is $v_{gr} = v_{NIR}^{gr} \cos \gamma$), the spectral intensity of the pump is given by

$$I_p(\omega) \propto \exp\left[-\left(\frac{\tau_p \omega}{2\sqrt{\ln 2}} \right)^2 \right]. \tag{16}$$

The pump pulse creates difference frequency (THz) waves determined by

$$E_{THz}(\Omega) \propto \Omega d(\Omega) E_p(\omega) \otimes E_p(\omega + \Omega), \tag{17}$$

where $\otimes$ means the cross correlation between two spectral components and $d(\Omega)$ is the nonlinear coefficient. The THz pulse shape at the crystal exit surface is given by

$$E_{THz}(t) = \int_\Omega \int_0^L E_{THz}(\Omega) \exp[-2\pi\alpha(\Omega)(L-z)] \cos$$
$$\times \left[\Omega\left(t - \frac{z}{v_{gr}} - \frac{L-z}{v_{THz}(\Omega)} \right) \right] dz d\Omega, \tag{18}$$

where L is the length of the crystal, $\alpha(\Omega)$ is the amplitude absorption coefficient, and z is measured from the entrance surface of the crystal. The nonlinear coefficient $d(\Omega)$ is calculated from a coupled electron–ion oscillator model [55]. It is

$$d(\Omega) = 1/2 \delta_{eee} \chi_e^2(\Omega) \chi_e(\Omega) + 1/2 \delta_{iee} \chi_i(\Omega) \chi_e^2(\Omega), \tag{19}$$

where χ_i and χ_e are the linear susceptibilities and δ_{iee} and δ_{eee} are the Miller delta coefficients for ions and electrons, respectively. $\chi_e(\Omega)$ is assumed to be constant, because the

electronic resonance frequency is in the visible (for semiconductors) or ultraviolet (for LN) region. For LN its value is $\chi_e(\Omega) = 3.674$. The frequency dependence of the ionic part of the second-order susceptibility $\chi_i(\Omega)$ is given by

$$\chi_i(\Omega) = \chi_{i0} \left| \frac{\omega_i^2}{\omega_i^2 - \Omega^2 + i\gamma\Omega} \right|, \tag{20}$$

where $\chi_{i0} = 23.36$, $\gamma = 0.34$ THz is the ionic damping constant, and $\omega_i/2\pi = 7.6$ THz is the ionic resonance frequency. $\delta_{iee} = 0.421$ (pm/V) and $\delta_{eee} = 0.761$ (pm/V) for LN [56]. In calculations performed for GaP the nonlinear coefficient given in [57] is used. We have no experimental information on the frequency dependence of the nonlinear coefficients for GaSe and ZnTe. For these materials Eqs. (19) and (20) are used with the known ω_i values, but keeping the value of γ in $d(\Omega)$ obtained for LN, and the whole expression is multiplied by the known ratio of d between LN, GaSe, and ZnTe (see Table 1).

The amplitude absorption $\alpha(\Omega)$ and refractive index $n(\Omega)$ values are calculated from the dielectric function $\varepsilon(\Omega)$ according to

$$\alpha(\Omega) = (\Omega/c)\mathrm{Im}\sqrt{\varepsilon(\Omega)}, \quad n(\Omega) = \mathrm{Re}\sqrt{\varepsilon(\Omega)}. \tag{21}$$

The dielectric function is described by a multiple oscillator model according to

$$\varepsilon(\Omega) = \varepsilon_\infty + \sum_k A_k \frac{\omega_k^2}{\omega_k^2 - \Omega^2 - 2i\gamma_k\Omega}, \tag{22}$$

where the high-frequency dielectric constant ε_∞, the resonance frequencies ω_k, and damping constants γ_k were obtained from literature [26,29,58]. For sLN the corresponding values at different temperature were obtained by fitting the measured absorption using a dielectric function containing two terms describing the first two polariton resonances around 252 and 276 cm^{-1}, and at least 10 terms describing other (mostly unidentified) resonances. This model takes into account dispersion and linear absorption in the THz range. It does not take into account dispersion and absorption of the pump pulse. However, these effects are very small for LN at 800 nm or longer pump wavelengths. For example, the stretching of a 100 fs long pulse in a 3 mm long LN crystal is only 3 fs. For the semiconductor materials these effects are larger, but neglecting them is still reasonable. Since in the model a few constants are omitted, the calculated electric field and THz energy values are obtained in arbitrary units. However, in the figures presented below, the values can be directly compared.

The main results of our calculations are presented in Figs. 7–9, which show THz waveforms, field amplitudes, and pulse energies for different temperatures and sLN crystal lengths. The most important conclusions we obtained [18,49] from performing calculations using the model presented above are the following.

(1) Because of the increasing dispersion and absorption with increasing THz frequency in sLN and semiconductors, the generated THz pulse shape depends on the selected THz frequency (for which velocity matching is
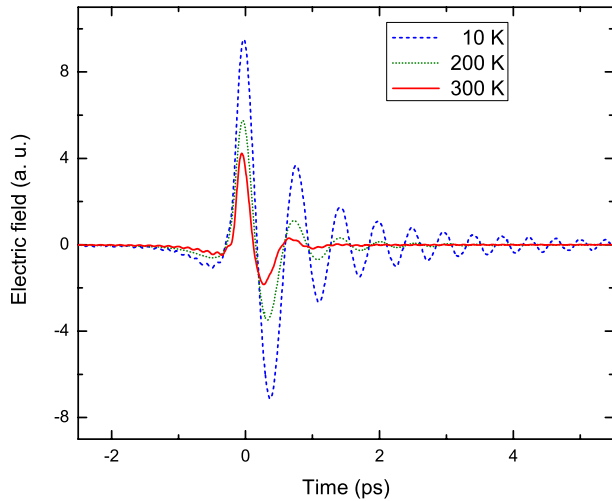
Fig. 7. (Color online) Calculated shapes of THz pulses generated in 2 mm long sLN by 140 fs long pump pulses for a 1 THz matched frequency at different temperatures. At low temperatures, polariton damping is low enough that small differences in polariton phase velocity lead to constructive superposition at the selected (1 THz) frequency but destructive interference at nearby frequencies, narrowing the THz spectral bandwidth. At high temperatures the THz propagation length is shorter, and nearby frequency components do not propagate far enough to go out of phase. The increased damping leads to a weaker and spectrally broader THz field.

fulfilled), the pump pulse duration, and the material, temperature, and length of the crystal. Nearly single-cycle THz pulses are generated at room temperature, low THz frequencies, short crystal lengths, and long pump pulses. On the other hand, long-lived oscillations, and correspondingly narrow THz spectra, are predicted for low temperatures, high velocity-matched frequencies, long crystal lengths, and short pump pulse durations, since at high THz frequencies the velocity-matching condition is met only for a narrow frequency range with a selected tilt angle.

(2) It is possible to tune the average frequency of the THz pulses just by changing the tilt angle γ of the pump intensity front to adjust the velocity matching. Using GaSe at room temperature or sLN at 10 K in this way,
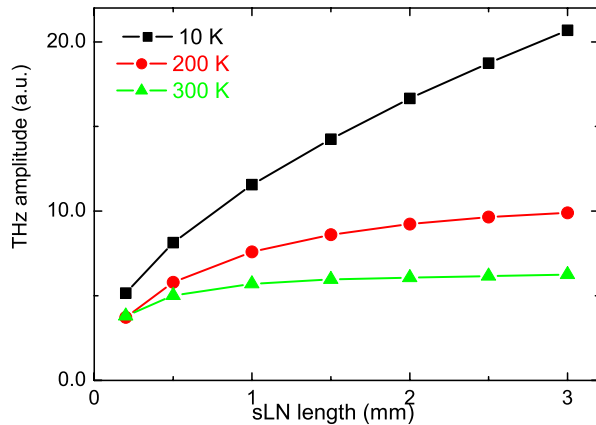

Fig. 8. (Color online) Calculated crystal length dependence of the electric field (peak-to-peak) amplitude of THz pulses generated in sLN by 140 fs duration pump pulses for 1 THz matched frequency at different temperatures.
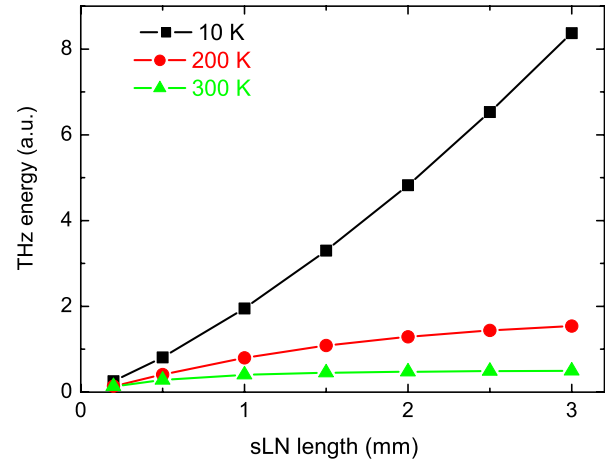

Fig. 9. (Color online) Calculated crystal length dependence of the energy of THz pulses generated in sLN by 140 fs long pump pulses for 1 THz matched frequency at different temperatures.

generation of THz pulses tunable in the 1–5 THz range is predicted. The bandwidth decreases from 1 THz to about 0.1 THz as the frequency increases. At lower than 2 THz matched frequency [because of the multiplication by Ω in Eq. (17)] the average frequency is larger than the matched one.

(3) Comparing the results obtained for different nonlinear crystals, it is predicted that for 2 THz matched frequency and 220 fs pump duration, the investigated crystals (GaSe, GaP, ZnTe, sLN) yield THz electric field amplitudes that are within in a factor of 2, but sLN generates the highest field. The THz energy generated by sLN is two times higher than the energy generated by the next best crystal, ZnTe. Note that these calculations assume the same pump pulse intensities, whereas in practice (as discussed above) substantially higher intensities can be used in sLN. For a 2 THz matched frequency it was found that there is an optimum crystal length for generating the highest electric field, because of the THz dispersion and absorption in the crystal. At room temperature in sLN it is 1 mm, while at 10 K temperature it is 2 mm. The THz energy depends less on the dispersion than the electric field amplitude. Because of this, longer crystals can be used for generating THz pulses with the highest energy.

Using the high-energy pulses from commercial amplified lasers available nowadays suggests using large excitation areas and crystal lengths, and in this case the maximum THz frequency shifts to lower values. Very recently we performed calculations for 1 THz matched frequency; 140 fs pump pulse duration was supposed. Figure 7 depicts the temporal shape of the THz pulses generated in 2 mm long sLN at 10, 200, and 300 K temperature. At room temperature the pulse is near single cycle, and even at 200 K the first period dominates. Similarly to the 2 THz case, the peak amplitude increases with decreasing temperature. However, because of the significantly reduced dispersion the THz pulse remains short even at 10 K temperature. Also, the reduced dispersion is the reason that, contrary to the 2 THz case, the peak amplitude of the electric field (see Fig. 8) and the THz energy (see

Fig. 9) increase monotonically with reduced temperature and do not drop at room temperature with increasing crystal length.

5. EXPERIMENTAL RESULTS OF THz PULSE GENERATION

In the first THz pulse generation experiments using tilted-pulse-front excitation as described here [14,18,48] the pump source was a 200 kHz system delivering 170 fs duration pulses with up to 2.6 μJ of energy. The pump spot size on the grating had less than 1 mm diameter. This meant that the pump spot at the sLN crystal was less than 0.5 mm vertically and about 0.7 mm horizontally. Accordingly the peak intensity in the crystal exceeded the 5 GW/cm^2 value. Using a sLN crystal with 2% Mg doping, THz pulses with energies of 30 pJ and 100 pJ were generated at room temperature and at 77 K temperature, respectively [48]. Replacing the crystal with one having only 0.6% Mg doping resulted in a more than three times increase of the energy [18]. Such an increase is expected because of the smaller THz absorption of the sLN with reduced doping level [31]. For the latter case the energy conversion efficiency was 1.7×10^{-4}, while the photon conversion efficiency exceeded 3% at 77 K. The average power of the generated radiation was 80 μW at low temperature and 20 μW at room temperature. The THz pulse shape was measured by electro-optic sampling [19] using a 0.6 mm thick ZnTe crystal. According to these measurements, at room temperature the THz pulse was essentially single cycle (see Fig. 10) with shorter than 1 ps duration. This short pulse duration means that the peak power of the THz pulses generated at room temperature was larger than 100 W and the intensity of the THz pulses in the sLN crystal was 30 kW/cm^2. In agreement with calculations ([18,49] and Subsection 4.B above), at low temperature the pulse duration was somewhat longer but still shorter than 2 ps. In this case the peak intensity exceeded 60 kW/cm^2, and the electric field strength reached 8 kV/cm. The generated THz beam was diffraction limited with a divergence of 50 mrad.

In agreement with the model calculations, at 10 K the reduced absorption made it possible [18] to tune the frequency of the THz pulses in the 1.0–4.4 THz range. The bandwidth of the pulses decreased from about 0.9 to 0.4 THz in this tuning range. The tuning was achieved by changing the tilt angle of the pump pulse front in the 59°–64° range.

A very important advantage of the tilted-pulse-front excitation geometry is that it makes scaling up the THz energy possible by increasing the pump energy and the excitation area. Figure 11 displays the energy of THz pulses generated in sLN by using pump lasers with significantly higher energy. In the experiment using a 1 kHz laser system with energy up to 0.5 mJ, a roughly four times larger excitation area was used than in the earlier experiment with 2.6 μJ pump pulse energy. As can be seen in Fig. 11, until about 10 μJ of pump energy, the THz energy increased quadratically with the pump energy. Above 100 μJ the pump energy dependence becomes linear. Various mechanisms for saturation of the conversion efficiency are currently under study. Although a saturation of the efficiency was observed for tilted-pulse-front excitation, the THz energy increased monotonically with pump energy, contrary to the case of line focus pumping. Using pump pulses having a few microjoules of energy, the efficiency of the line focus geometry was similar to the efficiency of the tilted-pulse-front geometry [47]. However, according to Fig. 11, for a few tens of microjoules of pump energy the efficiency of the line focus setup was significantly less than the efficiency of the tilted-pulse-front setup, and for greater than 30 μJ of pump energy the THz energy generated by the line focusing setup even drops. The limited excitation area for the line focus was the reason of this behavior. Because of this, the intensity of the pump becomes so high that even three-photon absorption of the pump may be efficient, causing increased THz absorption. Here clearly we can see the advantage of the tilted-pulse-front excitation for which the optical energy is distributed over a wide expanse of the crystal but the THz response that is generated remains concentrated within one or a few field cycles.
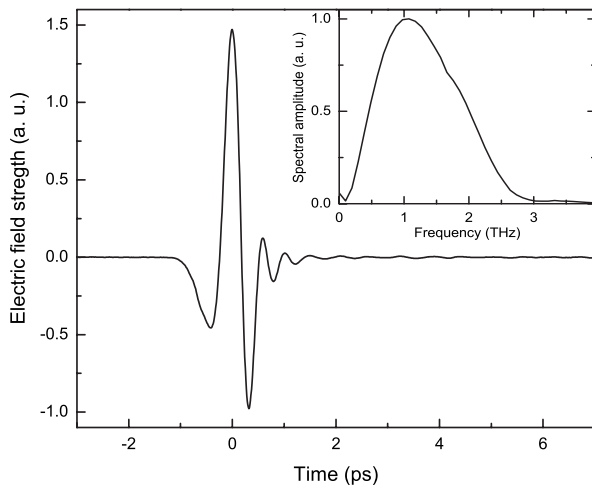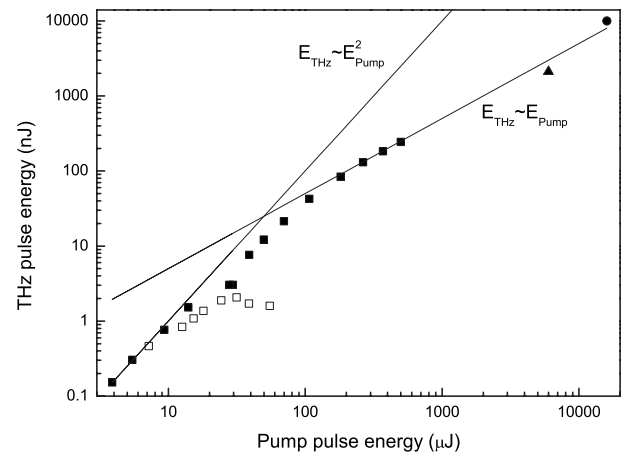

Fig. 10. Pulse shape of THz pulses generated at room temperature with a 200 kHz laser system. Inset, amplitude spectrum obtained by fast Fourier transform of the temporal shape.

Fig. 11. Dependence of the THz energy generated by a tilted pulse front on the pump energy for three different excitation areas: 1.2 mm^2 (filled squares), 9 mm^2 (triangle), and 30 mm^2 (circle). For comparison, open squares indicate THz energy generated by focusing to a 25 μm wide line creating a 0.04 mm^2 excitation area.

Very recently, using 6 mJ pump pulses at 1 kHz repetition rate, tilted-pulse-front excitation made possible [50] generation of THz pulses with at least 2.5 μJ of energy (see the triangle in Fig. 11) and correspondingly 2.5 mW average power. (The THz energy was measured by a pyroelectric energy meter. Its sensitivity is known at 1.06 μm. The sensitivity in the THz range may be significantly reduced [9], in which case the THz energy and average power were higher than the values given above.) According to electro-optic measurement (see Fig. 12), a single-cycle THz pulse was generated with a somewhat lower average frequency (0.85 THz, see the inset) than in the case of the microjoule pumping (see Fig. 10). The reason for the slight frequency shift may be the larger excitation area, and consequently the stronger effect of THz absorption at higher frequencies. One of the insets in Fig. 12 shows the beginning part of the temporal signal with 100 times vertical expansion, demonstrating that the signal-to-noise ratio is quite high at a repetition rate of 1 kHz.

In another very recent experiment [51], a 10 Hz Ti:sapphire laser system supplied pump pulses with 20 mJ of energy. In this case, using an irradiated area with 6 mm diameter, THz pulses with 10 μJ energy were generated (see the dot in Fig. 11). According to electro-optic measurement, the THz pulses were single-cycle with an average frequency of 0.7 THz. The THz peak power was as large as 5 MW, while the unfocused and focused (using a parabolic mirror pair with focal length ratio of 4) intensities reached 15 and 500 MW/cm^2, respectively. The focused size was less than 1 mm in diameter, and the electric field at the focus exceeded 600 kV/cm. The photon conversion efficiency was as high as 45% and resulted in a strong distortion to the red side of the transmitted pump spectrum. With a simple calculation it is possible [51] to calculate the internal photon conversion efficiency from the average redshift of the pump spectrum. A value of 800% was obtained. The two main reasons for the large discrepancy between the calculated internal and measured external (45%) photon conversion efficiency are the reflection loss of about 50% and the THz absorption. The

absorption significantly decreases on cooling of the crystal [31]. Both according to experiment [18] and model calculation (see Fig. 9), a 3–5 times increase in the THz energy can be achieved through cryogenic cooling of the sLN crystal. Some increase in the THz coupling into free space might be achieved through partial index matching with silicon or a similar material, as has been demonstrated recently [59,60].

In recent years, femtosecond fiber laser systems have become a more efficient and user-friendly alternative to Ti:sapphire laser systems. Yb-doped fiber laser systems using chirped pulse amplification have become available commercially. For THz generation using a 1035 nm pump wavelength, GaP is the most commonly used material because it allows collinear velocity matching [61] and avoids direct two-photon absorption. In a very recent study [62] a GaP waveguide was pumped by the 14 W average power pulses of a 25 MHz repetition-rate Yb-doped fiber laser-amplifier system. The low THz absorption of GaP and the exact velocity matching achieved by the appropriate choosing of the cross side of the waveguide made it possible to use a crystal as long as 6 mm. The generated average THz power reached 120 μW. As a consequence of the waveguide dispersion two-cycle pulse shapes were observed.

In our recent study [38] we compared the achieved THz pulse energies by using GaP, sLN, and ZnTe as nonlinear materials for the optical rectification process with an Yb-doped bulk laser system as pump source. The main results are summarized in Fig. 13.

At low pump energy the THz energy shows quadratic pump energy dependence for all materials as indicated by the curves. At intermediate pump levels the dependence becomes linear in ZnTe, and at high pump energies the THz energy shows strong saturation for both ZnTe and GaP. In contrast, the behavior in sLN is still quadratic at intermediate pump levels and becomes linear at high pump levels without showing saturation. The saturation in ZnTe and GaP can be attributed to two- and three-photon absorption in the respective materials. The free carriers generated by multiphoton absorption cause strong THz absorption. Owing to its large bandgap of 3.8 eV [39] neither two- nor three-photon absorption is
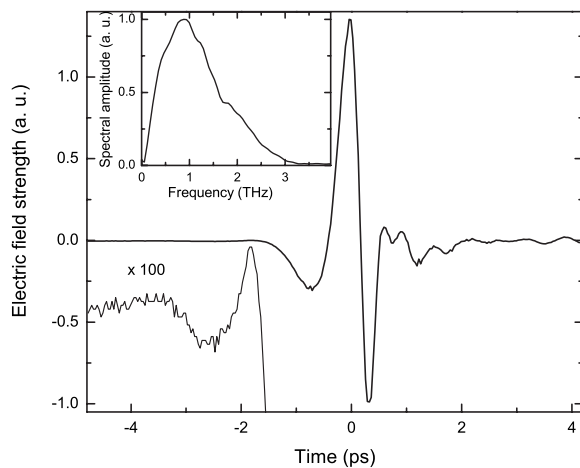

Fig. 12.   Pulse shape of THz pulses generated at room temperature with a 1 kHz laser system and 6 mJ pump pulse energy. Insets, amplitude spectrum of the pulse, and beginning part of the temporal shape with 100 times vertical expansion.
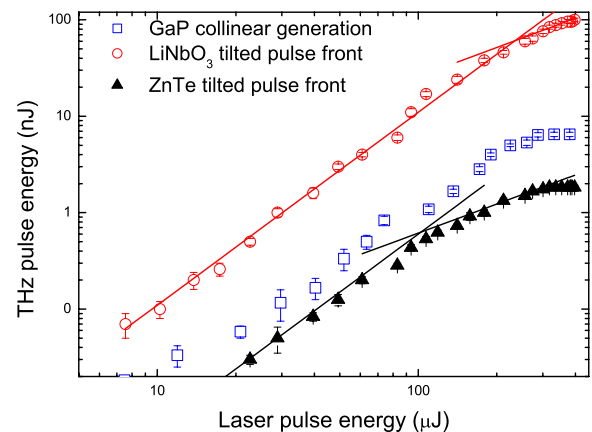

Fig. 13.   (Color online) THz pulse energy versus pump energy, using a Yb pump laser and sLN (circles), GaP (squares) and ZnTe (triangles) nonlinear materials.

possible in sLN. Beside the large FOM value of sLN (see Table 1), the absence of two- and three-photon absorption in this material is the reason for the ten times more efficient generation in this material than in GaP.

Very recently we generated single-cycle THz pulses at a 1 MHz repetition rate. Using 10 μJ energy pulses from an IMPULSE (Clark-MXR, Inc.) femtosecond Yb-fiber laser system and sLN nonlinear crystal, single-cycled THz pulses with 0.5 nJ energy were generated. Accordingly the average THz power exceeded 0.5 mW. With the specified 20 μJ energy output from this laser system, we anticipate 2 mW THz power, since with these pumping conditions we are in the quadratic regime.

6. GENERATION OF SHAPED THz PULSES

The THz pulses generated by using ultrashort pump pulses and tilted-pulse-front excitation have single-cycle or near-single-cycle temporal shapes and consequently broad spectral bandwidths. However, many possible applications of THz pulses need narrower bandwidths. Such pulses have been generated by using optical rectification in periodically domain inverted materials, such as periodically poled LN (PPLN) [41], in optically contacted multilayer or diffusion-bonded GaAs [63], and in LN polaritonic elements including resonators [64,65] and bandgap structures [66]. Narrowband THz waves also have been generated in homogeneous LN crystals, and characterized outside or within the generating crystals by use of temporally [67] or spatially [68,69] periodic excitation. Although in principle some of these techniques would be suitable for generating even arbitrary shaped THz pulses, those methods in which the structure of the nonlinear material determines the pulse shape offer limited versatility, since they are not reconfigurable. It was demonstrated that both spatial [68,69] and temporal [67] modulation of the pump pulse is easily applicable for producing arbitrary shaped THz pulses in homogeneous LN crystals. Temporal pulse shaping also was used for narrowband polariton generation in a LN THz resonator [65] and for low-power THz waveform synthesis with a photoconducting dipole antenna [70]. None of these papers reported THz pulse generation at the microjoule level.

The combination of tilted pulse front excitation and temporal shaping of the pump is very promising for narrowband or arbitrarily shaped THz pulse production in the nanojoule to microjoule energy range. This should combine the advantages of femtosecond visible–NIR pulse shaping techniques [71] with the high THz generation efficiency of the tilted-pulse-front excitation geometry. Very recently we reported a simple demonstration of this concept [50]. Shaped optical pulses were produced by reflecting 100 fs, 2 mJ, 800 nm pulses from partial (50%) and high reflectors in close ($\sim$100 μm) proximity. The resulting optical pulse sequences with equidistant delay and exponentially decreasing energy were used to excite THz pulse sequences in sLN crystal in a tilted-pulse-front setup. The frequency of the THz pulse was directly determined by the temporal delay between the pulses in the optical pulse sequence. It was possible to change this frequency simply by changing the separation between the 50% and the 100% reflectivity mirrors. In order to reduce

the THz absorption, the sLN crystal was cooled to 80 K. The energy of the THz waveforms approached 1 μJ. This result clearly demonstrates the efficiency of the concept. Construction of a high-energy, arbitrarily shaped THz waveform source with a reconfigurable Fourier plane femtosecond pulse shaper [71] and the 6 mJ, 1 kHz laser system is now under way. We anticipate shaped THz waveforms with several microjoules of energy. Intense shaped THz fields may enable THz nonlinear spectroscopy and coherent control not only of electronic responses with strong THz transition dipoles, such as those in Rydberg atoms [72] and semiconductor quantum well intersubband transitions [73], but of ionic and molecular responses including polar lattice vibrations, molecular orientational motions, and collective structural and electronic rearrangements that might result from them.

7. FUTURE PROSPECTS

As we mentioned in Section 1, using the tilted-pulse-front excitation method we were able to produce THz pulses in sLN having 1000 times larger energy [15] than the energy of THz pulses generated in ZnTe [8] by using the same pump pulse energy. This huge difference in conversion efficiency cannot be explained by the difference in nonlinear coefficients. The more important reason for the much better performance of sLN for high-energy THz generation is that it is a dielectric with higher bandgap [39] than the energy of the two photons of the 800 nm pump pulse. Because of this, for sLN much higher pump intensity can be used than for semiconductors, resulting in higher THz pulse energy and higher conversion efficiency. For example, in [15] close to 2×10^{11} W/cm^2 pump intensity was used, but only 4×10^9 W/cm^2 (8 mm beam diameter) or 5×10^8 W/cm^2 (24 mm beam diameter) was used in [8]. It is worth noting that even with the larger beam diameter more than 30% of the pump light was absorbed in the 2 mm long ZnTe crystal because of its high (4.2 $\times 10^9$ cm/W) [74] two-photon absorption coefficient. The charges created in this way caused significantly larger THz absorption than the THz absorption of sLN.

Owing to the problem of two-photon absorption and the resulting induced THz absorption, recently the possibility of applying pump sources with longer wavelengths was investigated [63], and photon conversion efficiency of up to 3×10^{-4} was achieved. This is an attractive aim, since it can make possible [63] the use of femtosecond fiber lasers that are more compact, robust, and economic than Ti:sapphire lasers. However, according to the fourth and fifth columns of Table 1, at the 1.55 μm wavelength of the Er^{+3} fiber laser, the group velocity of the pump is larger than the velocity of the THz radiation for all of the indicated nonlinear crystals. For the currently most popular ZnTe material the pump group velocity exceeds the THz phase velocity even when an Yb-doped fiber laser is used. In these cases tilted pulse front excitation will be necessary in order to achieve velocity matching. Therefore use of tilted-pulse-front excitation is expected to have broad importance in enabling the general application of fiber lasers for THz pulse generation.

The generation of shaped microjoule energy THz pulses with field levels in the megavolt per centimeter range will

enable novel applications in THz nonlinear coherent spectroscopy and coherent control. Recent observations of THz nonlinearities [75] including self-phase modulation [76] based on LN lattice anharmonicities foreshadow the possibilities. Multidimensional THz spectroscopy analogous to that currently conducted in the mid-infrared [77] and THz coherent control over macroscopic and mesoscopic material structure such as ferroelectric phases and domain orientations and the responses of correlated electron systems [78], multiferroics, and other multifunctional materials should emerge. THz control over low-frequency electronic resonances with strong transition dipoles in Rydberg atoms [72] and semiconductor intersubband levels [73] has been demonstrated, and with the high-amplitude shaped THz fields that can now be generated, control over other electronic responses such as charge transport in electron-transfer chemical systems and in electrical components including single-electron devices also may become possible. A new window on large-amplitude lattice vibrations, interionic and intermolecular motions in liquids, glasses, and partially disordered systems, as well as the structural rearrangements that involve these motions, will be opened.

8. CONCLUSION

We have presented a brief review of a unique approach to THz generation through which materials with high nonlinear coefficients can be used effectively despite their high THz refractive indices, which prevent phase matching in the usual collinear geometry. The use of tilted-intensity-front optical excitation permits generation of single- or few-cycle THz waveforms with high field amplitudes, energies, and average power levels. The approach is also naturally amenable to combination with femtosecond pulse shaping methods for generation of high-power shaped THz outputs. These characteristics will spur the broad emergence of nonlinear THz coherent spectroscopy and coherent control.

Tilted-pulse-front THz generation has been demonstrated to date by using 800 nm and 1.035 μm excitation light in lithium niobate and (with 1.035 μm pumping) zinc telluride crystals. We anticipate extension of tilted-pulse-front THz generation to fiber-based laser systems and a variety of dielectric and semiconductor nonlinear materials that may be pumped by them.

ACKNOWLEDGMENTS

REFERENCES AND NOTES

1. B. Ferguson and X-C. Zhang, "Materials for terahertz science and technology," Nat. Mater. **1**, 26–33 (2002).
2. C. A. Schmuttenmaer, "Exploring dynamics in the far-infrared with terahertz spectroscopy," Chem. Rev. (Washington, D.C.) **104**, 1759–1780 (2004).
3. Y. Shen, T. Watanabe, D. A. Arena, C.-C. Kao, J. B. Murphy, T. Y. Tsang, X. J. Wang, and G. L. Carr, "Nonlinear cross-phase modulation with intense single-cycle terahertz pulses," Phys. Rev. Lett. **99**, 043901 (2007).
4. D. You, R. R. Jones, P. H. Bucksbaum, and D. R. Dykaar, "Generation of high-power sub-single-cycle 500-fs electromagnetic pulses," Opt. Lett. **18**, 290–292 (1993).
5. A. Dreyhaupt, S. Winnerl, T. Dekorsy, and M. Helm, "High-intensity terahertz radiation from a microstructured large-area photoconductor," Appl. Phys. Lett. **86**, 121114 (2005).
6. B. B. Hu, X.-C. Zhang, and D. H. Auston, "Free-space radiation from electro-optic crystals," Appl. Phys. Lett. **56**, 506–508 (1990).
7. K. Reimann, R. P. Smith, A. M. Weiner, T. Elsaesser, and M. Woerner, "Direct field-resolved detection of terahertz transients with amplitudes of megavolts per centimeter," Opt. Lett. **28**, 471–473 (2003).
8. T. Löffler, T. Hahn, M. Thomson, F. Jacob, and H. G. Roskos, "Large-area electro-optic ZnTe terahertz emitters," Opt. Express **13**, 5353–5362 (2005).
9. F. Blanchard, L. Razzari, H.-C. Bandulet, G. Sharma, R. Morandotti, J.-C. Kieffer, T. Ozaki, M. Ried, H. F. Tiedje, H. K. Haugen, and F. A. Hegmann, "Generation of 1.5 μJ single-cycle terahertz pulses by optical rectification from a large aperture ZnTe crystal," Opt. Express **15**, 13212–13220 (2007).
10. A. Nahata, A. S. Weling, and T. F. Heinz, "A wideband coherent terahertz spectroscopy system using optical rectification and electro-optic sampling," Appl. Phys. Lett. **69**, 2321–2323 (1996).
11. R. M. Koehl and K. A. Nelson, "Terahertz polaritonics: automated spatiotemporal control over propagating lattice waves," Chem. Phys. **267**, 151–159 (2001).
12. R. M. Koehl and K. A. Nelson, "Coherent optical control over collective vibrations traveling at lightlike speeds," J. Chem. Phys. **114**, 1443–1446 (2001).
13. T. Feurer, J. C. Vaughan, and K. A. Nelson, "Spatiotemporal coherent control of lattice vibrational waves," Science **299**, 374–377 (2003).
14. J. Hebling, G. Almási, I. Z. Kozma, and J. Kuhl, "Velocity matching by pulse front tilting for large area THz-pulse generation," Opt. Express **10**, 1161–1166 (2002).
15. A. G. Stepanov, J. Kuhl, I. Z. Kozma, E. Riedle, G. Almási, and J. Hebling, "Scaling up the energy of THz pulses created by optical rectification," Opt. Express **13**, 5762–5768 (2005).
16. R. L. Sutherland, *Handbook of Nonlinear Optics* (Marcel Dekker, 1996), pp. 87–88.
17. We note that Eq. (5) includes a factor of 4 that was missing in Eq. (5) of [18]. We thank a reviewer for drawing our attention to this problem.
18. J. Hebling, A. G. Stepanov, G. Almási, B. Bartal, and J. Kuhl, "Tunable THz pulse generation by optical rectification of ultrashort laser pulses with tilted pulse fronts," Appl. Phys. B **78**, 593–599 (2004).
19. Q. Wu and X.-C. Zhang, "Ultrafast electro-optic field sensors," Appl. Phys. Lett. **68**, 1604–1606 (1996).
20. M. Schall, M. Walther, and P. Uhd Jepsen, "Fundamental and second-order phonon processes in CdTe and ZnTe," Phys. Rev. B **64**, 094301 (2001).
21. D. T. F. Marple, "Refractive Index of ZnSe, ZnTe, and CdTe," J. Appl. Phys. **35**, 539–542 (1964).
22. E. D. Palik, *Handbook of Optical Constants of Solids* (Academic, 1985), pp. 429–444.
23. D. Grischkowsky, S. Keiding, M. van Exter, and C. Fattinger, "Far-infrared time-domain spectroscopy with terahertz beams of dielectrics and semiconductors," J. Opt. Soc. Am. B **7**, 2006–2015 (1990).
24. D. F. Nelson and E. H. Turner, "Electro-optic and piezoelectric coefficients and refractive index of gallium phosphide," J. Appl. Phys. **39**, 3337–3343 (1968).
25. Ref. [22], pp. 445–464.
26. K. Wynne and J. J. Carey, "An integrated description of

terahertz generation through optical rectification charge transfer, and current surge," Opt. Commun. **256**, 400–413 (2005).

27. V. I. Sokolov and V. K. Subashiev, "Linear electroptical effect in gallium selenide," Sov. Phys. Solid State **14**, 178–183 (1972).

28. K. L. Vodopyanov and L. A. Kulevskii, "New dispersion relationships for GaSe in the 0.65–18 μm spectral region," Opt. Commun. **118**, 375–378 (1995).

29. N. Piccioli, R. Le Toullec, M. Mejatty, and M. Balkanski, "Refractive index of GaSe between 0.45 micrometer and 330 micrometers," Appl. Opt. **16**, 1236–1238 (1977).

30. M. Nakamura, S. Higuchi, S. Takekawa, K. Terabe, Y. Furukawa, and K. Kitamura, "Optical damage resistance and refractive indices in near-stoichiometric MgO-doped LiNbO$_3$," Jpn. J. Appl. Phys., Part 1 **41**, L49–L51 (2002).

31. L. Pálfalvi, J. Hebling, J. Kuhl, A. Péter, and K. Polgár, "Temperature dependence of the absorption and refraction of Mg-doped congruent and stoichiometric LiNbO3 in the THz range," J. Appl. Phys. **97**, 123505 (2005).

32. M. Schall, H. Helm, and S. R. Keiding, "Far infrared properties of electro-optic crystals measured by THz time-domain spectroscopy," Int. J. Infrared Millim. Waves **20**, 595–604 (1999).

33. A. Schneider, M. Neis, M. Stillhart, B. Riuz, R. U. A. Khan, and P. Günter, "Generation of terahertz pulses through optical rectification in organic DAST crystals: theory and experiment," J. Opt. Soc. Am. B **23**, 1822–1835 (2006).

34. F. Pan, G. Knöpfle, C. Bosshard, S. Follonier, R. Spreiter, M. S. Wong, and P. Günter, "Electro-optic properties of the organic salt 4-*N*,*N*-dimethylamino-4′-*N*′-methyl-stilbazolium tosylate," Appl. Phys. Lett. **69**, 13–15 (1996).

35. M. Walther, K. Jensby, S. R. Keiding, H. Takahashi, and H. Ito, "Far-infrared properties of DAST," Opt. Lett. **25**, 911–913 (2000).

36. W. D. Johnston, Jr. and I. P. Kaminov, "Contributions to optical nonlinearity in GaAs as determined from Raman scattering efficiencies," Phys. Rev. **188**, 1209–1211 (1969).

37. A. Schneider, M. Stillhart, and P. Günter, "High efficiency generation and detection of terahertz pulses using laser pulses at telecommunication wavelengths," Opt. Express **14**, 5376–5384 (2006).

38. M. C. Hoffmann, K.-L. Yeh, J. Hebling, and K. A. Nelson, "Efficient terahertz generation by optical rectification at 1035 nm," Opt. Express **15**, 11706–11713 (2007).

39. D. Redfield and W. J. Burke, "Optical absorption edge of LiNbO$_3$," J. Appl. Phys. **45**, 4566–4571 (1974).

40. L. Pálfalvi, J. Hebling, G. Almási, Á. Péter, K. Polgár, K. Lengyel, and R. Szipócs, "Nonlinear refraction and absorption of Mg doped stoichiometric and congruent LiNbO$_3$," J. Appl. Phys. **95**, 902–908 (2004).

41. Y.-S. Lee, T. Meade, M. DeCamp, T. B. Norris, and A. Galvanauskas, "Temperature dependence of narrow-band terahertz generation from periodically poled lithium niobate," Appl. Phys. Lett. **77**, 1244–1246 (2000).

42. P. A. Tipler, *Physics for Scientists and Engineers* (W. H. Freeman, 1999).

43. J. Hebling, "Derivation of the pulse-front-tilt caused by angular dispersion," Opt. Quantum Electron. **28**, 1759–1763 (1996).

44. D. H. Auston, "Subpicosecond electro-optic shock waves," Appl. Phys. Lett. **43**, 713–715 (1983).

45. D. H. Auston, K. P. Cheung, J. A. Valdmanis, and D. A. Kleinman, "Cherenkov radiation from femtosecond optical pulses in electro-optic media," Phys. Rev. Lett. **53**, 1555–1558 (1984).

46. D. A. Kleinman and D. H. Auston, "Theory of electrooptic shock radiation in nonlinear optical media," IEEE J. Quantum Electron. **20**, 964–970 (1984).

47. A. G. Stepanov, J. Hebling, and J. Kuhl, "THz generation via optical rectification with ultrashort laser pulse focused to a line," Appl. Phys. B **81**, 23–26 (2005).

48. A. G. Stepanov, J. Hebling, and J. Kuhl, "Efficient generation of subpicosecond terahertz radiation by phase-matched optical rectification using ultrashort laser pulses with tilted pulse fronts," Appl. Phys. B **83**, 3000–3002 (2003).

49. B. Bartal, I. Z. Kozma, A. G. Stepanov, G. Almási, J. Kuhl, E. Riedle, and J. Hebling, "Toward generation of μJ range sub-ps THz pulses by optical rectification," Appl. Phys. B **86**, 419–423 (2007).

50. K.-L. Yeh, J. Hebling, M. C. Hoffmann, and K. A. Nelson, "Generation of high average power 1 kHz shaped THz pulses via optical rectification," Opt. Commun. (to be published).

51. K.-L. Yeh, J. Hebling, M. C. Hoffmann, and K. A. Nelson, "Generation of 10 μJ ultrashort terahertz pulses by optical rectification," Appl. Phys. Lett. **90**, 171121 (2007).

52. O. E. Martinez, "Pulse distortions in tilted pulse schemes for ultrashort pulses," Opt. Commun. **59**, 229–232 (1986).

53. I. Z. Kozma, G. Almási, and J. Hebling, "Geometrical optical modeling of femtosecond setups having angular dispersion," Appl. Phys. B **76**, 257–261 (2003).

54. D. W. Ward, E. R. Statz, K. A. Nelson, R. M. Roth, and R. M. Osgood, "Terahertz wave generation and propagation in thin-film lithium niobate produced by crystal ion slicing," Appl. Phys. Lett. **86**, 022908 (2005).

55. D. H. Auston and M. C. Nuss, "Electrooptical generation and detection of femtosecond electrical transients," IEEE J. Quantum Electron. **24**, 184–196 (1988).

56. G. D. Boyd and M. A. Pollack, "Microwave nonlinearities in anisotropic dielectrics and their relation to optical and electro-optical nonlinearities," Phys. Rev. B **7**, 5345–5359 (1973).

57. A. Leitenstorfer, S. Hunsche, J. Shah, and M. C. Nuss, "Detectors and sources for ultrabroadband electro-optic sampling: experiment and theory," Appl. Phys. Lett. **74**, 1516–1518 (1999).

58. D. F. Parsons and P. D. Coleman, "Far infrared optical constants of gallium phosphide," Appl. Opt. **10**, 1683–1685 (1971).

59. K. Kawase, J.-i. Shikata, H. Minamide, K. Imai, and H. Ito, "Arrayed silicon prism coupler for a terahertz-wave parametric oscillator," Appl. Opt. **40**, 1423–1426 (2001).

60. M. Theuer, G. Torosyan, C. Rau, R. Beigang, K. Maki, C. Otani, and K. Kawase, "Efficient generation of Cherenkov-type terahertz radiation from a lithium niobate crystal with a silicon prism output coupler," Appl. Phys. Lett. **88**, 071122 (2006).

61. Q. Wu and X.-C. Zhang, "7 terahertz broadband GaP electro-optic sensor," Appl. Phys. Lett. **70**, 1784–1786 (1997).

62. G. Chang, C. J. Divin, J. Yang, M. A. Musheinish, S. L. Williamson, A. Galvanauskas, and T. B. Norris, "GaP waveguide emitters for high power broadband THz generation pumped by Yb-doped fiber lasers," Opt. Express **15**, 16308–16314 (2007).

63. G. Imeshev, M. E. Fermann, K. L. Vodopyanov, M. M. Fejer, X. Yu, J. J. Harris, D. Bliss, and D. Weyburne, "High-power source of THz radiation based on orientation-patterned GaAs pumped by a fiber laser," Opt. Express **14**, 4439–4444 (2006).

64. N. S. Stoyanov, T. Feurer, D. W. Ward, E. R. Statz, and K. A. Nelson, "Direct visualization of a polariton resonator in the THz regime," Opt. Express **12**, 2387–2396 (2004).

65. D. W. Ward, J. D. Beers, T. Feurer, E. R. Statz, N. Stoyanov, and K. A. Nelson, "Coherent control of phonon-polaritons in a terahertz resonator fabricated with femtosecond laser machining," Opt. Lett. **29**, 2671–2673 (2004).

66. D. W. Ward, E. R. Statz, J. D. Beers, T. Feurer, J. D. Joannopoulos, R. M. Roth, R. M. Osgood, K. J. Webb, and K. A. Nelson, "Polaritonics in complex structures: confinement, bandgap materials, and coherent control," in *Ultrafast Phenomena XIV*, T. Kobayashi, T. Okada, T. Kobayashi, K. A. Nelson, and S. De Silvestri, eds. (Springer-Verlag, 2005), pp. 298–300.

67. J. Ahn, A. V. Efimov, R. D. Averitt, and A. J. Taylor,

"Terahertz waveform synthesis via optical rectification of shaped ultrafast laser pulses," Opt. Express **11**, 2486–2496 (2003).

68. T. F. Crimmins, N. S. Stoyanov, and K. A. Nelson, "Heterodyned impulsive stimulated Raman scattering of phonon–polaritons in $LiTaO_3$ and $LiNbO_3$," J. Chem. Phys. **117**, 2882–2896 (2002).

69. A. G. Stepanov, J. Hebling, and J. Kuhl, "Generation, tuning, and shaping of narrow-band, picosecond THz pulses by two-beam excitation," Opt. Express **12**, 4650–4658 (2004).

70. Y. Liu, S.-G. Park, and A. M. Weiner, "Terahertz waveform synthesis via optical pulse shaping," IEEE J. Sel. Top. Quantum Electron. **2**, 709–719 (1996).

71. A. M. Weiner, "Femtosecond pulse shaping using spatial light modulators," Rev. Sci. Instrum. **71**, 1929–1969 (2000).

72. J. Ahn, D. N. Hutchinson, C. Rangan, and P. H. Bucksbaum, "Quantum phase retrieval of a Rydberg wave packet using a half-cycle pulse," Phys. Rev. Lett. **86**, 1179–1182 (2001).

73. B. E. Cole, J. B. Williams, B. T. King, M. S. Sherwin, and C. R. Stanley, "Coherent manipulation of semiconductor quantum bits with terahertz radiation," Nature **410**, 60–63 (2001).

74. R. De Salvo, A. A. Said, D. J. Hagan, E. W. van Stryland, and M. Sheik-Bahae, "Infrared to ultraviolet measurements of two-photon absorption and n_2 in wide bandgap solids," IEEE J. Quantum Electron. **32**, 1324–1333 (1996).

75. T. Hornung, K. L. Yeh, and K. A. Nelson, in *Ultrafast Phenomena XV*, P. Corkum, D. Jonas, R. J. D. Miller, A. M. Weiner, eds. (Springer-Verlag, 2007), pp. 772–774.

76. J. Hebling, K.-L. Yeh, M. C. Hoffmann, and K. A. Nelson, "High power THz generation, THz nonlinear optics, and THz nonlinear spectroscopy," IEEE J. Sel. Top. Quantum Electron. (to be published).

77. M. Khalil, N. Demirdoven, and A. Tokmakoff, "Coherent 2D IR spectroscopy: molecular structure and dynamics in solution," J. Phys. Chem. A **107**, 5258–5279 (2003).

78. M. Rini, R. Tobey, J. Itatani, Y. Tomioka, Y. Tokura, R. W. Schoenlein, and A. Cavalleri, "Control of the electronic phase of a manganite by mode-selective vibrational excitation," Nature **449**, 72–74 (2007).